# Supercritical mixing and combustion in rocket propulsion

**By J.-P. Hickey AND M. Ihme**

## 1. Motivation and objectives

The modeling of trans- and supercritical mixing and combustion introduces considerable challenges for predictive rocket combustion simulations. Near the critical point, the thermo-physical properties of fluids undergo drastic changes that occur in the absence of a phase change. At these extreme pressure conditions, the repulsive atomic forces become important enough to overcome the surface tension and create a single-phase, dense fluid that shares the properties of a gas (e.g., high diffusivity) and a liquid (e.g., high density). In the transcritical regime, mixing is primarily a diffusion driven process in which the thermo-physical properties are non-linear functions of local pressure and temperature. Given the liquid-like density near the critical point, the fluid is prone to extreme density gradients in an otherwise continuous medium. For example, at a pressure of 5.5 MPa, the density of transcritical oxygen decreases, on average, by over 46 kg/m$^3$ per degree Kelvin between 150 K and 160 K. Similarly, the specific heat at constant pressure varies by a factor of 10 within this same range, see Figure 1. This highly non-linear behavior near the critical point is just one example of the inability of the ideal gas law to relate the thermo-physical states. This strongly non-linear behavior is at the heart of the challenges in real fluid modeling and simulation.

The need to accurately model trans- and supercritical flows is particularly acute in liquid rocket engines (LRE) where high-density cryogenic fuels and oxidizers are injected into high-pressure combustion chambers. At supercritical operating pressures, the subcritical temperature of the liquid fuel and oxidizer must increase to a supercritical state —with the consequential thermo-physical variations —before combustion can occur (see the phase diagram representation in Figure 2). The accurate modeling of the real fluid effects on the fuel/oxidizer mixing is important for characterizing the subsequent combustion in these engines. However, from a design standpoint, the subversive effects of the strong non-linear behavior of the fluid require special consideration. Rocket engines are characterized by the concurrent importance of a multiplicity of complex, highly coupled physical phenomena, which affect the design parameter space. Most critical to the design is the predictive determination of the onset of combustion instabilities, which constrain the operating conditions of the engine. Combustion instabilities arise because of the strong coupling between the fluid, heat release, and acoustic modes. It is hypothesized that the transcriticality of the injected fluid may greatly influence the stability of the system as acoustic pressure oscillations near the critical point have an important effect on the flow and mixing (Chehroudi 2012). The current design cycle of rocket engines rests on an expensive trial-and-error approach, with the expectation of identifying the stability bounds of the system; computational fluid dynamics are currently used only as complementary verification. An increased use and dependability of numerical tools in the design process can only be achieved through a better understanding of the coupling

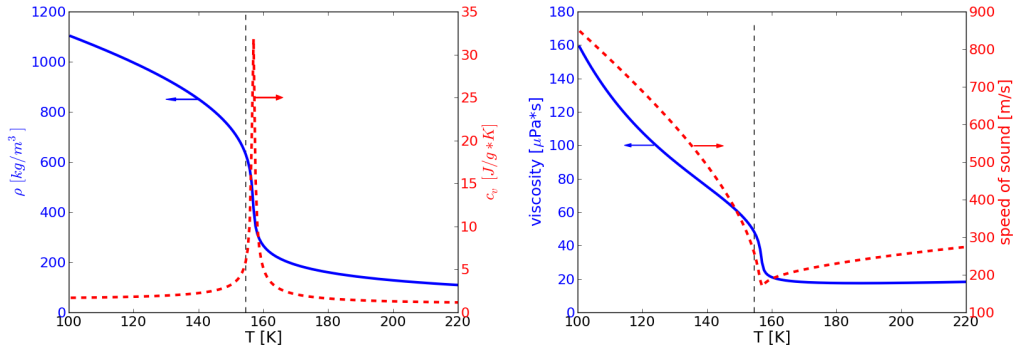


Figure 1: Temperature dependant variation of physical properties of $O_2$ at supercritical pressure ($p = 5.5$ MPa). (a) density (full, blue line) and specific heat capacity (dashed, red line); (b) viscosity (full, blue line) and speed of sound (dashed, red line).

between fluid dynamics, chemical kinetics, heat transfer and acoustic —particularly in the trans- and supercritical regimes.

The study of trans- and supercritical reacting and non-reacting flows has garnered much interest, especially since the early 1990s. The high-pressure, non-reacting jet is one of the simplest —although still physically relevant —setups used to characterize the strongly non-linear thermo-physical behavior. An experimental setup, conducted at the Deutsches Zentrum für Luft- und Raumfahrt (DLR) by Mayer *et al.* (1998), highlighted the strongly diffusive nature of the supercritical jet in a series of insightful visualizations. This seminal work opened the door to subsequent advances in the physical understanding and experimental methods of non-reacting jets (Oschwald & Schik 1999; Chehroudi *et al.* 2002; Habiballah *et al.* 2006). These works showed that in the supercritical regime, the liquid propellant does not atomize since the surface tension becomes negligible. Instead, the propellant and oxidizer undergo a complex gas/gas-like mixing with high diffusivity, which is very sensitive to pressure and temperature perturbations. The combustion in the supercritical regime has also received some attention from the rocket community. Mayer & Tamura (1995), on the DLR rig, showed a visualization of the supercritical combustion of $LO_X/GH_2$. Candel *et al.* (1998) investigated the reacting case of a high-pressure shear coaxial injector jet flame. Other cryogenic fuels, such as $CH_4$, have also recently been studied (Yang *et al.* 2007; Lux & Haidn 2009).

The pioneering numerical work in supercritical mixing and combustion in rocket engines can be attributed to Oefelein & Yang (1998). Bellan's group (Bellan 2000; Miller *et al.* 2001; Okong'o & Bellan 2002*b*, 2003; Bellan 2006; Lelle *et al.* 2007; Masi *et al.* 2013) has conducted a series of canonical studies focusing, among others, on the direct numerical simulation of temporally evolving mixing layers of a heptane and a nitrogen stream. Resting on the foundations of previous thermodynamic studies (e.g., Harstad *et al.* 1997), they defined simple mixing rules, derived a clear set of thermodynamically consistent fluid properties, investigated Dufour and Soret effects in supercritical flows (Miller *et al.* 2001), addressed the handling of characteristic boundary conditions (Okong'o & Bellan 2002*a*) and the sub-grid scale modeling (Selle *et al.* 2007) in the supercritical environment. Other groups have studied transcritical nitrogen injection using Reynolds-Average

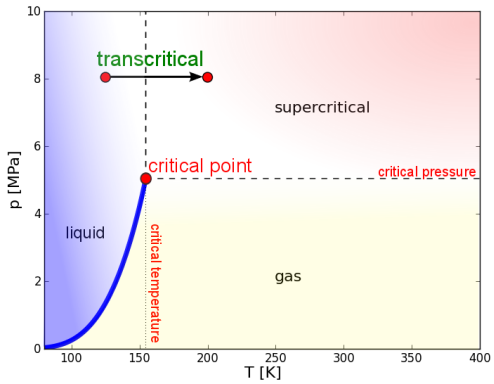


Figure 2: Phase diagram of $O_2$. The saturation line data is from the National Institute of Technology and Standards (NIST).

Navier-Stokes (Cutrone *et al.* 2006, 2010), large eddy simulation (Schmitt *et al.* 2010; Niedermeier *et al.* 2013) and direct numerical simulations (Terashima *et al.* 2011; Terashima & Koshi 2012, 2013). A number of reacting high-pressure simulations have been attempted, most notably as part of the *Rocket Combustion Modeling Workshop* held in 2001 and 2006. The challenges associated with modeling high-pressure combustion is most clearly evidenced in the comparative simulation work by Tucker *et al.* (2008); a number of independent numerical studies were conducted with significantly different simulation outcomes. Recent foundational work by Lacaze & Oefelein (2012) has investigated the use of the flamelet formulation for supercritical flow.

The objective of the current work is to report on the development a high-fidelity numerical framework for the study of sub-, trans- and supercritical mixing and combustion in rocket engines. The work is written to archive the implementation steps of the real fluid models within *CharLES*$^x$, the in-house, unstructured, large-eddy simulation code used at the Center for Turbulence Research at Stanford. This paper is organized as follows. In Section 2, the thermodynamic formulation for the equation of state and departure functions are presented; Section 3 details the numerical implementation for the non-reacting and the flamelet/progress-variable (FPV) model. Results for non-reacting and reacting cases are presented in Section 4.

## 2. Modeling the real fluid effects

### 2.1. *Equation of state*

In the vicinity of the critical point, the intermolecular repulsive forces modify the relationship between pressure, density, and temperature. These molecular forces render the ideal gas law inapplicable for modeling the thermodynamic state. Historically, van der Waal was the first to connect the fundamental state of the molecular forces to the deviation of the ideal gas law. His quadratic equation of state has formed the basis for many subsequent variations of higher-order equations of state (EoS); a detailed description of the commonly used state equations can be found in standard thermodynamic references (see Prausnitz *et al.* 1999; Poling *et al.* 2001). Although most of the equations of state are able to capture the important thermo-physical variations, the computational tractability

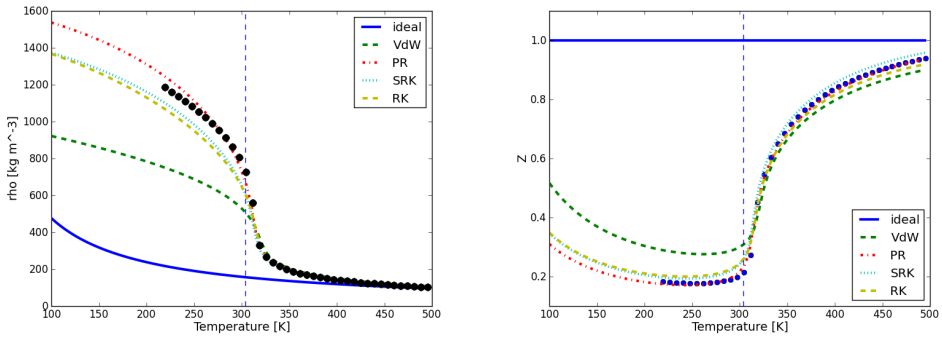


(a) (b)

Figure 3: Comparison of various state equations for carbon dioxide at 9 MPa (reduced pressure of 1.219). Density variation (a) and compressibility factor, $\mathcal{Z}$, (b) with temperature. Comparison among ideal gas law, Van der Waals EoS (VdW), Peng-Robinson EoS (PR), Soave-modified Redlich-Kwong EoS (SRK), and Redlich-Kwong EoS (RK). Symbols represent the values from the National Institute of Standards and Technology (NIST).

plays a considerable role in selecting the appropriate EoS. For numerical efficiency, the state equations should be simple enough to allow for a rapid computation of the thermodynamic states while simultaneously accounting for the full complexity of the non-linear relationship between the variables. A comparison of various analytical equations of state is presented in Figure 3.

In the present implementation, the cubic equation of state offers an acceptable compromise between the conflicting requirements of accuracy and computational tractability. The cubic Peng-Robinson (Peng & Robinson 1976) equation of state was chosen as it is accurate, particularly close to the critical point (Miller *et al.* 2001). The Peng-Robinson equation of state takes the form:

$$p = \frac{\mathcal{R}T}{\mathcal{V} - B_m} - \frac{A_m}{\mathcal{V}\left(\mathcal{V} + B_m\right) + B_m\left(\mathcal{V} - B_m\right)}, \tag{2.1}$$

where $\mathcal{V}$ and $\mathcal{R}$ represent, respectively, the molar volume and universal gas constant. The coefficients $A_m$ and $B_m$ are evaluated using the critical properties and temperature of the fluid. As these equations are developed for pure fluids, mixing rules are applied to treat multi-species mixtures with $N_s$ species. The computation of the coefficients are weighted with their molar fraction such that (Miller *et al.* 2001)

$$A_m = \sum_{\alpha=1}^{N_s}\sum_{\beta=1}^{N_s} X_\alpha X_\beta A_{\alpha\beta}, \qquad B_m = \sum_{\alpha=1}^{N_s} X_\alpha B_\alpha, \tag{2.2}$$

where:

$$A_{\alpha\beta} = 0.457236\frac{\left(\mathcal{R}T_{c,\alpha\beta}\right)^2}{p_{c,\alpha\beta}}\left[1 + C_{\alpha\beta}\left(1 - \sqrt{T/T_{c,\alpha\beta}}\right)\right]^2, \tag{2.3}$$

$$B_\alpha = 0.077796\mathcal{R}T_{c,\alpha\alpha}/p_{c,\alpha\alpha}, \tag{2.4}$$

$$C_{\alpha\beta} = 0.37464 + 1.54226\Omega_{\alpha\beta} - 0.26992\Omega_{\alpha\beta}^2. \tag{2.5}$$

The critical properties of the mixtures are evaluated using the following mixing rules (Harstad *et al.* 1997):

$$\begin{aligned}
T_{c,\alpha\beta} &= \sqrt{T_{c,\alpha\alpha} T_{c,\beta\beta}}\,(1 - k_{\alpha\beta}) \\
\mathcal{V}_{c,\alpha\beta} &= 1/8 \left[\mathcal{V}_{c,\alpha\alpha}^{1/3} + \mathcal{V}_{c,\beta\beta}^{1/3}\right]^3 \\
p_{c,\alpha\beta} &= Z_{c,\alpha\beta}\,(\mathcal{R} T_{c,\alpha\beta}/\mathcal{V}_{c,\alpha\beta}) \\
\mathcal{Z}_{c,\alpha\beta} &= 1/2\,(\mathcal{Z}_{c,\alpha\alpha} + \mathcal{Z}_{c,\beta\beta}) \\
\Omega_{c,\alpha\beta} &= 1/2\,(\Omega_{c,\alpha\alpha} + \Omega_{c,\beta\beta})\,,
\end{aligned}$$

for $\alpha, \beta = 1, 2, \ldots, N_s$, $k_{\alpha\beta}$ is the binary interaction parameter. In the above equations, the repeated indices represent the properties of the pure species.

### 2.2. *Thermodynamic and transport properties*

A thermodynamically consistent formulation is developed by partially deriving the above equation of state in order to construct the appropriate departure functions. Departure functions relate the difference between the high-pressure thermodynamic state and its value at standard atmospheric pressure. As such, the true internal energy of the fluid is the sum of the energy at atmospheric pressure and the departure function for internal energy. Figure 4 illustrates the enthalpy departure function in the supercritical state. Because the thermodynamic quantities such as internal energy, specific heat or enthalpy are state properties, they depend only on their initial and final state, not on the path between these states. Therefore, the departure functions are exact descriptions of the real fluid effects —the only approximation arises from the choice of the equation of state. The departure functions (noted here with the prefix $\mathcal{D}$) are re-written in terms of known thermodynamic quantities. Based on the Peng-Robinson state equation, (2.1), the departure function for the molar internal energy is

$$\mathcal{D}e = e\,(\mathcal{V}, T) - e_0\,(T) = \left(\frac{\frac{\partial A_m}{\partial T}\big|_{\mathcal{V},Y_k}\, T - A_m}{2\sqrt{2} B_m}\right) \ln\left(\frac{\mathcal{V} + \left(1 - \sqrt{2}\right) B_m}{\mathcal{V} + \left(1 + \sqrt{2}\right) B_m}\right). \tag{2.6}$$

Similarly, departure functions for the molar specific heat capacity at constant volume can be computed:

$$\mathcal{D}c_v = c_v\,(\mathcal{V}, T) - c_v^0\,(T) = -\frac{T\,\frac{\partial^2 A_m}{\partial T^2}\Big|_{\mathcal{V},Y_k}}{2\sqrt{2} B_m} \ln\left(\frac{\mathcal{V} + \left(1 - \sqrt{2}\right) B_m}{\mathcal{V} + \left(1 + \sqrt{2}\right) B_m}\right). \tag{2.7}$$

The exact derivatives of the Peng-Robinson coefficients and further thermodynamic properties (such as isentropic compressibility and speed of sound) can be found in Miller *et al.* (2001).

The method by Chung *et al.* (1984, 1988) is used to evaluated the dynamic viscosity of the mixture. There are two formulations of the Chung *et al.* model depending on the pressure of the system; both are derived from the Chapman-Enskog equation which accounts for the intermolecular forces. In the implementation of these models, attention should be paid to the non-standard units used for determining the coefficients. Here, for sake of brevity, only the low-pressure formulation is presented; the high-pressure correction to this equation can by found in standard references (Chung *et al.* 1988; Poling *et al.* 2001).

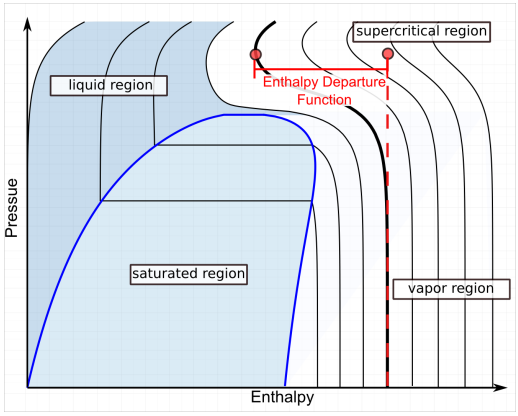


Figure 4: Illustration of the departure function of enthalpy in state-space. Isothermal lines are shown.

The low-pressure viscosity $\mu$ (in units of $\mu$P) is computed as

$$\mu = 40.785 F_c \frac{\sqrt{M_m T}}{\mathcal{V}_{cm}^{2/3} \Omega_v}, \tag{2.8}$$

where

$$F_c = 1 - 0.275\omega_m + 0.059035\mu_{rm}^4 + \kappa_m \ , \tag{2.9}$$

and

$$\Omega_v = \frac{A}{T^{*-B}} + C\exp\left(-DT^*\right) + E\exp\left(-FT^*\right), \tag{2.10}$$

where $T^* = 1.2593T_r = 1.2593T/T_c$. $M_m$ and $\mathcal{V}_{cm}$ are, respectively, the molecular weight (g/mol) and critical molar volume (cm$^3$/mol). The details of the remaining coefficients can be found in Chung *et al.* (1988).

## 3. Numerical implementation

The real fluid modules were integrated into *CharLES$^x$*, an in-house, unstructured, finite-volume large-eddy simulation code developed at the Center for Turbulence Research at Stanford University. The spatially averaged compressible Navier-Stokes equations are solved in a fully conservative form with a third-order explicit Runge-Kutta time advancement. The governing equations are solved using a hybrid approach that switches between a low-dissipation centered (fourth-order) and lower-order schemes [either first-order or second-order essentially non-oscillatory (ENO) scheme] (Khalighi *et al.* 2010). The lower-order schemes are activated only in regions of high local density variation using a threshold-based sensor. The sub-grid scale stresses are modeled following Vreman (2004). Two distinct implementations of the real fluid model are present in *CharLES$^x$*. For non-reactive simulations, an iterative approach is used to compute pressure and temperature from the transported internal energy and density (see details in Section 3.1). For the reacting cases, a flamelet-progress variable (FPV) method (Pierce & Moin 2004; Ihme *et al.* 2005) with presumed beta-PDF closure is extended to account for the real fluid effects and to include departure functions and compressibility factors as pre-tabulated variables (details in Section 3.2).

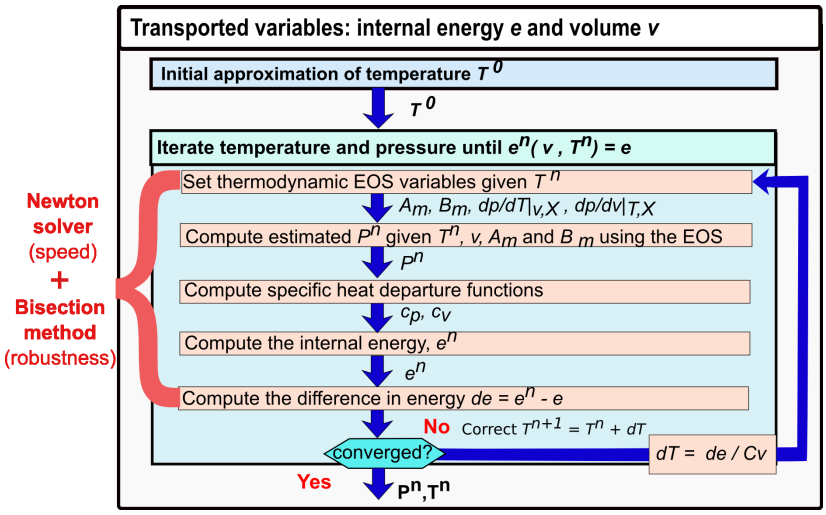


Figure 5: Iterative algorithm to determine the correct thermodynamic state given the transported density and internal energy.

### 3.1. *Pure-mixing of multi-species fluids*

As mentioned above, the Navier-Stokes equations are solved in a fully conservative form. The solution vector $\mathbf{\Phi} = [\rho, \rho u_i, \rho E, \rho Y_1 ... \rho Y_{N_s}]$ where $i$ spans the three spatial dimensions and the total number of the species, $N_s$. The total energy, $E$, represents the sum of the internal and kinetic energy. From these conservative variables, the thermodynamic properties must be computed. For a calorically perfect gas, the temperature is directly computed from the internal energy for the given composition. Knowing temperature and density, the pressure is found from the ideal gas law. For non-ideal fluids, the energy is a function of two thermodynamic variables for a given composition. Because the only other thermodynamic variable in the solution vector is the density, an iterative procedure must be adopted to compute either pressure or temperature. The remaining thermodynamic variable is then computed from the non-linear equation of state. The details of the iterative algorithm are shown Figure 5 and explained next.

From the transported variables at a given composition, the internal energy and molar volume are computed. To initiate the algorithm, an estimate of temperature must be provided. An estimate based on the ideal gas law is acceptable, although the initial error can be significant near the critical point. In the present implementation, a fixed value of temperature is used as an initial guess; the temperature from the previous time-step could also be used as an initial guess. Given the estimated temperature, $T^0$, the thermodynamic derivatives (e.g., $dp/dT$) and constants ($A_m$ and $B_m$) can be computed. These quantities are used to calculate the estimated pressure, $p^n$, from Eq. (2.1). The specific heats at constant pressure, $c_p$, and volume, $c_v$ can then be estimated. The definition of all the thermodynamic variables allows for the computation of the internal energy. The difference between the transported and estimated internal energy is used to determine if the algorithm is converged. If the relative difference between the transported and estimated internal energy is below a user-defined threshold (default threshold of $10^{-6}$), the algorithm is completed and returns the pressure and temperature. Otherwise, the procedure continues. A Newton solver is used for the computational efficiency of the code.

For the temperature correction, we use the definition of specific heat at constant volume to improve the efficiency and accuracy of our code: $c_v = \frac{\partial e}{\partial T}\big|_v$. Using the corrected temperature and transported molar volume, we restart the algorithm until convergence is achieved. If the convergence is not achieved after 50 iterations or if the temperature departs from a reasonable range ($T = [50, 4000]$ K), the algorithm is re-initialized, and a bisection method is used for robustness.

### 3.2. *Combustion and flamelet tabulation*

For reacting cases, a flamelet/progress variable (FPV) model accounts for the chemical kinetics by pre-computing and tabulating the source terms of the transported equations. In order to populate the chemical table, the flamelet equations in the mixture fraction space are computed using an in-house extension to FlameMaster (Pitsch 2006) to account for real fluid effects described above.

By solving the compressible form of the Navier-Stokes equations with FPV, an overdetermined set of thermodynamic variables arise. The solution vector of the governing equations defines two thermodynamic variables, namely the density and the internal energy. These thermodynamic variables are sufficient to fully characterize the thermodynamic state of the flow (as shown in the non-reacting case). Similarly, the solution of the flamelet equations also describes the full thermodynamic state of the counter diffusion flame at a constant base pressure, $p^{\text{tab}}$. In order to avoid overdetermining the system with decoupled energy terms (tabulated and transported), Terrapon *et al.* (2010) proposed a flamelet modeling strategy that corrects the tabulated temperature by accounting for the difference in tabulated and transported energy. The extension to this approach for the real fluid effects is detailed here.

The premise of the methodology proposed by Terrapon *et al.* (2010) lies in the correction of the tabulated energy by the difference between the transported and tabulated temperatures:

$$\begin{aligned} e(T,P) = e^{\text{tab}}(T^{\text{tab}}, p^{\text{tab}}) + \Delta e = \\ e^{\text{tab}}(T^{\text{tab}}, p^{\text{tab}}) + \int_{T^{\text{tab}}}^{T} \frac{\mathcal{R}}{\gamma\,(T) - 1} dT, \end{aligned} \tag{3.1}$$

where $\mathcal{R}$ is the gas constant of the mixture. In the real fluid formulation, the tabulated internal energy (per unit mass) represents the sum of the low pressure internal energy, $e_o\,(T)$ and the departure function, $\mathcal{D}e(T,p)$. Therefore, we have

$$e^{\text{tab}}(T^{\text{tab}}, p^{\text{tab}}) = e_o^{\text{tab}}(T) + \mathcal{D}e^{\text{tab}}(T^{\text{tab}}, p^{\text{tab}}). \tag{3.2}$$

To be formally exact, the Eq. (3.1) would need to account for the change in the departure function of internal energy for the change of temperature and pressure between $T$ and $T^{\text{tab}}$ and $p$ and $p^{\text{tab}}$, respectively. Although, such an iterative procedure to correct the departure function could be envisioned, it would require a significant computational expense for a consistent evaluation of the internal energy. In the present implementation, this secondary departure function correction is neglected.

In order to correct the energy about the tabulated state, Terrapon *et al.* (2010) assumes a linear dependance of specific heat ratio such that

$$\gamma\,(T) = \gamma^{\text{tab}} + a_\gamma \left(T - T^{\text{tab}}\right). \tag{3.3}$$

This is an important assumption that is prone to error, particularly if $\left(T - T^{\text{tab}}\right)$ is large or $T$ and $p$ are near the critical point. Since $\gamma$ is only used for the ideal gas correction in

Eq. (3.1), the standard, low-pressure definition of the specific heat ratio is tabulated:

$$\gamma^{\text{tab}} = \frac{c_p}{c_v}. \tag{3.4}$$

The convenient linearization allows to explicitly rewrite the energy Eq. (3.1) as

$$e = e_0^{\text{tab}} + \mathcal{D}e^{\text{tab}} + \frac{\mathcal{R}}{a_\gamma} \ln\left(1 + \frac{a_\gamma \left(T - T^{\text{tab}}\right)}{\gamma^{\text{tab}} - 1}\right). \tag{3.5}$$

An explicit relationship between $T$ and $e$ is then achieved.

The real fluid effects of the thermodynamic variables are computed by tabulating the local value of the compressibility factor, $\mathcal{Z} = pv/(\mathcal{R}T)$. As such, given the local temperature and density, the non-linearities of the equation of state are accounted for within the compressibility factor. Therefore

$$p = \mathcal{Z}\rho\mathcal{R}T. \tag{3.6}$$

This computationally efficient approach accounts for the full non-linearity among the thermodynamic variables. Finally, the high pressure viscosity (based on Chung's model, see above) is also tabulated.

## 4. Numerical simulations

Two cases are presented to illustrate the capabilities of *CharLES*$^x$ to model high-pressure, non-reacting and reacting cases.

### 4.1. *Non-reacting case: Transcritical nitrogen jet*

The injection of a cryogenic nitrogen jet into a supercritical pressurized vessel was studied as the first test case in the second International Rocket Combustion Modeling workshop (Telaar *et al.* 2001). The experimental work was conducted at DLR (Branam & Mayer 2002) to study the transcritical behavior of cryogenic fluids. As it is one of the most well-established experiments, it has been used as a benchmark validation case by many groups. It has been investigated using Reynolds-averaged Navier-Stokes (RANS) Eq. (Cutrone *et al.* 2006, 2010), large-eddy simulations (Schmitt *et al.* 2010; Selle & Schmitt 2010; Hickey *et al.* 2013; Niedermeier *et al.* 2013; Ma *et al.* 2013), and direct numerical simulation (Terashima & Koshi 2013). The setup consists of an injector (2.2 mm diameter) injecting nitrogen into a large pressurized vessel at 4.0 MPa at a constant velocity of 5.04 m/s. In the experimental setup, the diameter of the pressurized vessel is large compared with that of the injector diameter. Consequently, wall effects are deemed to be negligible. Therefore, we select the domain size based on the simulation by Terashima *et al.* (2011) as $100D$ by $400D$ where, $D$ is the diameter of the injector. The temperature of the injected nitrogen is 126.9 K, whereas the temperature of the fluid within the vessel is 298 K. We recall that the critical properties of pure nitrogen are $p_c = 3.398$ MPa and $T_c = 126.19$ K. Figure 6 (a) shows the relative change in volume for a given relative change in pressure (in absolute value) at the base pressure of the setup. A clear spike in sensitivity is noted between temperatures of 130K and 140K, reaching a maximum of about 5.5. This peak implies that a very small relative change in pressure will result in a significant variation in the density. The two-dimensional simulations are conducted at two levels of grid refinement. The coarse and regular mesh have respectively 66,000 and 225,000 control volumes. This corresponds to over 400 points (clustered near the injector)

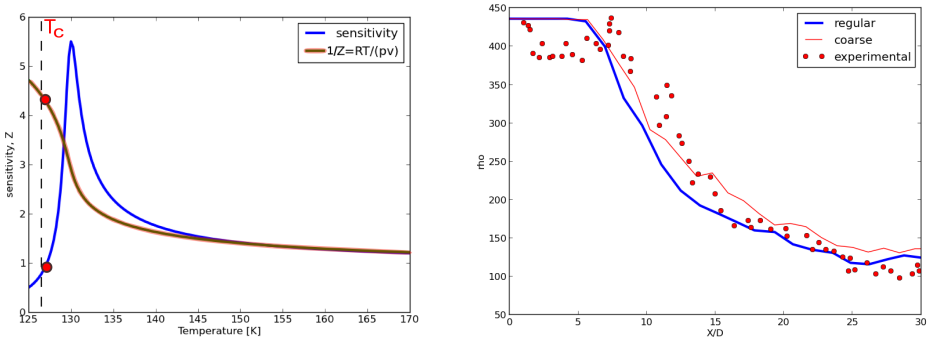


(a) (b)

Figure 6: (a) Effect of temperature on transcritical nitrogen; the inverse compressibility $1/\mathcal{Z} = \mathcal{R}T/p\mathcal{V}$ and relative sensitivity $\frac{p}{\mathcal{V}} \left.\frac{\partial \mathcal{V}}{\partial p}\right|_T$ at 4.0 MPa (from the NIST database). (b) The numerical simulation results with the experimental experimental data by Branam & Mayer (2002).


Figure 7: Instantaneous results of the nitrogen injector. (a) velocity magnitude ($0 \leq |\mathbf{u}| \leq 5.6m/s$); (b) temperature ($125.6 \leq T \leq 306.7$ K)

in the streamwise direction and 50 points within the injector; the minimum spacing in the injector is $1/100D$. Another 250 points are used to discretize the domain above and below the injector plane. The walls are adiabatic and characteristic inflow and outflow conditions are used.

The centerline density profile is shown in Figure 6 (b) for the two grid qualities investigated. Although error estimates on the experimental measurements are lacking in the original work, the present simulations appear to capture the general trend of the density profile and scalar mixing quite well. The exact location of the average breakup appears to occur slightly ahead of the experimental data, although, in the far field, a very good agreement is achieved. Spurious numerical oscillations complicate this seemingly simple simulation. Even if the centerline profile is well captured, local pressure oscillations arise from the strong non-linearity of the equation of state and the large density gradients. To account for these non-physical oscillations, numerical viscosity needs to be added. Previous works have used artificial dissipation with user-defined coefficients (Schmitt *et al.* 2010; Terashima & Koshi 2013) or with flux-limiters (Niedermeier *et al.* 2013). In the present work, a dual-threshold approach was used. The density-based sensor switches between a second-order ENO and first-order scheme to suppress the oscillations. The instantaneous snapshots, as well as the min/max thermodynamic values, are presented in Figure 7.

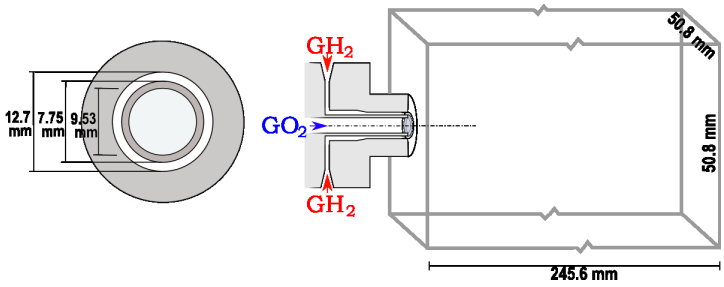


Figure 8: Setup for Penn State combustor (not to scale).

### 4.2. *Reacting case: Single injector Penn State combustor*

A high-pressure $GO_2/GH_2$ single injector reacting case is studied. The setup is based on the Penn State combustor presented by Foust *et al.* (1996). The principal dimensions of the uni-element, co-axial injector and combustion chamber are presented in Figure 8, the nominal operating conditions are reported in Table 1; the near-wall purge gas is neglected for computational simplicity. The Reynolds number of the coaxial injector is 109,000 and 64,500 respectively for the $O_2$ and $H_2$ streams based on the radius and bulk flow velocity. Although the conditions are not supercritical, this setup was investigated as it offers a complete set of quantitative validation data. Similar extensive data is unavailable in supercritical combustion cases. Admittedly, the compressibility factor, $\mathcal{Z}$, is 0.9997 and 0.9918, respectively in the fuel and oxidizer streams. Real fluid effects, although limited, are accounted for in the tabulated departure function terms, the compressibility factor and viscosity.

Flamelets were computed using the high-pressure $H_2/O_2$ mechanism by Burke *et al.* (2012) with a modified version of FlameMaster (Pitsch 2006) to account for real fluid effects. The flamelet/Progress-Variable chemical table is constructed using the mixture fraction, the mixture fraction variance, and a progress variable. The progress variable is defined as the sum of the mass fractions of hydrogen $H_2$ and oxygen $O_2$.

The three-dimensional computational domain is gridded using 1.15 and 3.2 million control volumes for the coarse and regular simulations. The block structured, O-grid mesh consists of 75 and 100 control volumes, respectively, in the radial and circumferential directions of the central injector. The outer coaxial injector has 25 control volumes with a minimum grid spacing of $5 \times 10^{-5}$ m at the wall. The extent of the coaxial injector is $8.5R$ upstream of the combustion chamber in order to achieve a turbulent injection of the fuel and oxidizer streams. At the inlet of the coaxial injector, synthetic turbulence is generated based on a digital filtering technique (Touber & Sandham 2009).

An instantaneous snapshot of the flame is shown in Figure 9. The time-averaged statistics are presented in Figs. 10-11. The statistics are averaged over approximately 5 characteristic time-scales (based on the injector diameter and fuel velocity) starting from $t = 2.0269$ms, which corresponds to over 2 flow through times on the regular grid —it should be noted that the flow was initialized with a lower resolution simulation result, which had undergone at least 8 flow through times. The time-average results are then circumferentially averaged using 100 individual planes. The mean velocity profile in Figure 10 (top) shows good agreement with the experimental data. On the lower quality mesh, the peak velocity was slightly lower owing to the extra numerical dissipation suggesting that grid convergence has not yet been achieved. The turbulence statistics in Figure 10

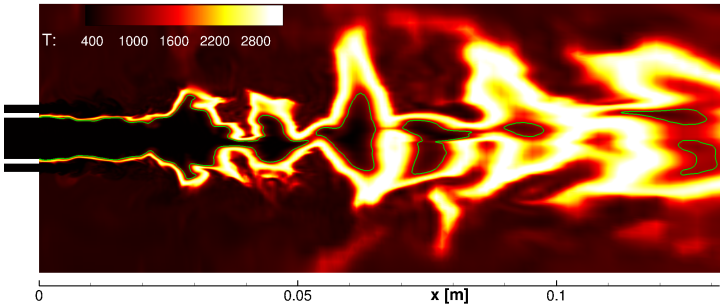


Figure 9: Instantaneous snapshot of the temperature field at $t = 2.0269$ms.

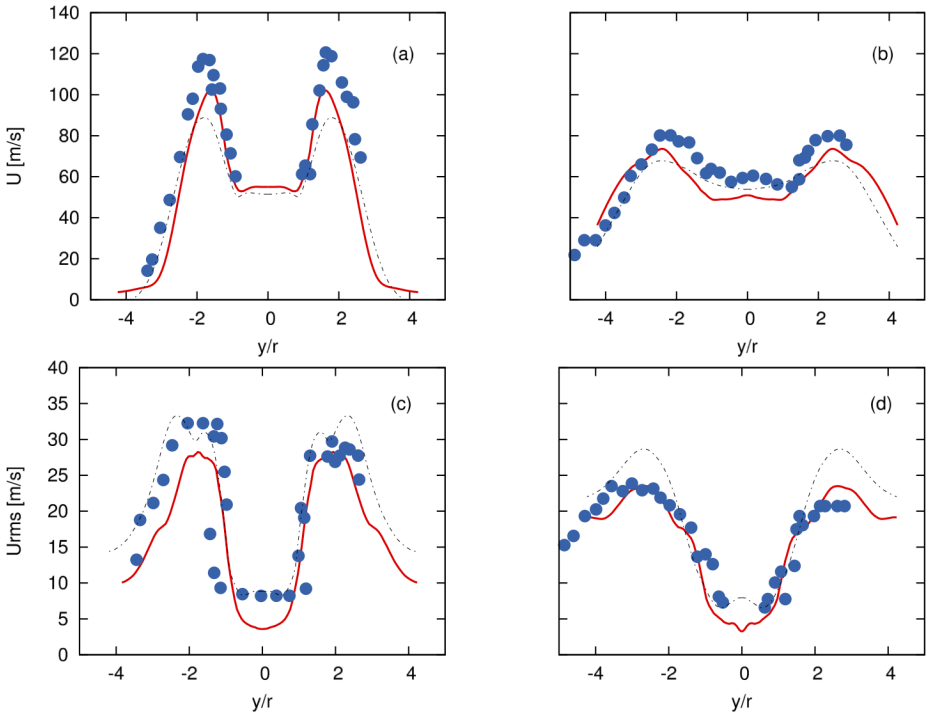


Figure 10: Mean velocity profile (top) and streamwise root-mean square profile (bottom) at 25.4 (a)-(c) and 50.8 mm (b)-(d). Results from the coarse (dash-dotted line) and regular (thick red line) simulations are compared with the experimental data by Foust *et al.* (1996).

(bottom) also show good agreement with the experimental data. The molar composition in Figure 11 shows a worse agreement on the finer grid, especially at 50.8 mm. This suggests that the combustion might occur upstream of this measurement location in the regular grid simulation.

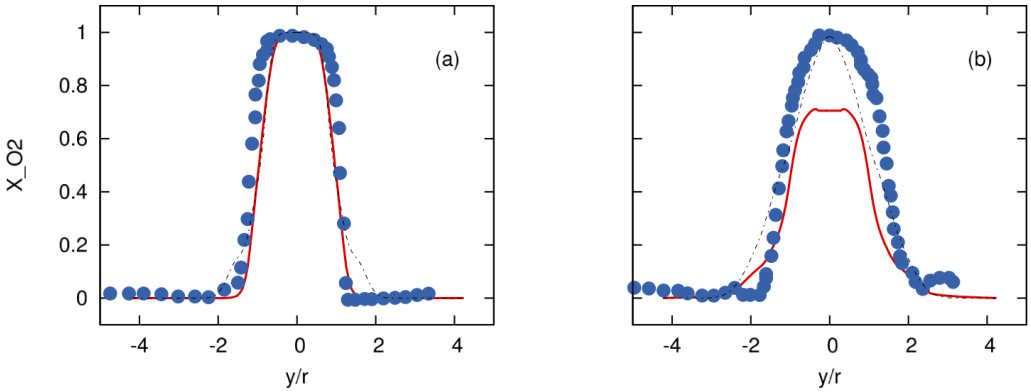


Figure 11: Oxygen molar fraction at 25.4 (a) and 50.8 mm (b). The large-eddy simulation results are compared to the data by Foust *et al.* (1996).

| Pressure | $\dot{m}_{GH_2}$ | $\dot{m}_{GO_2}$ | $U_{GH_2}$ | $U_{GO_2}$ | $T_{GH_2}$ | $T_{GO_2}$ |
|---|---|---|---|---|---|---|
| 1.29 | $1.03 \times 10^{-2}$ | $4.2 \times 10^{-2}$ | 177 | 51 | 297 | 297 |

Table 1: Nominal operating conditions of the Penn State combustor Foust *et al.* (1996). The base pressure (MPa), mass flow rates of fuel and oxidizer (kg$\cdot$ s$^{-1}$), fuel and oxidizer velocity (m$\cdot$ s$^{-1}$) and temperature (K).

## 5. Conclusion and future work

In this brief, we report on the implementation of the real fluid extensions to *CharLES*$^x$. A conceptually distinct implementation was needed for the pure-mixing and the FPV model combustion case. For the non-reacting simulations, a Newton-Raphson based iterative algorithm is used to determine the temperature from the transported density and energy. For the reacting simulations, an extended flamelet table is used that tabulates the departure functions, viscosity as well as the compressibility factor. These tabulated parameters are used to correct the transported thermodynamic properties, the approach is an extension of the work by Terrapon *et al.* (2010).

The real fluid extension to *CharLES*$^x$ was used to investigate a non-reacting and a reacting case. This preliminary work illustrates the capability *CharLES*$^x$ to capture the important physics in a typical rocket engine configuration. Several aspects require further consideration. From a numerical point of view, the stability of the numerics remains tenuous and requires dissipative schemes to avoid spurious numerical oscillations. Although the dissipative schemes solve the numerical stability issue, the added dissipation drastically modifies the underlying flow physics —especially in transitioning flows. In the combustion case, the underlying assumptions needed for the correction of the energy equation requires a more thorough quantification of the error, particularly in the transcritical and cryogenic regimes. In addition, simulations need to be conducted on supercritical setups, despite the lack of quantitative validation data. This work opens the opportunities for future inquiries for supercritical mixing and combustion.

**Acknowledgments**

This work was in part supported by NASA's Marshall Space Flight Center. The authors are grateful for the help of Peter C. Ma for help in testing and validation of the real fluid methods for pure mixing in *CharLES*$^x$. The authors acknowledge computing time on the Certainty cluster at Stanford (MRI-R2 NSF Award 0960306).

## REFERENCES

Bellan, J. 2000 Supercritical (and subcritical) fluid behavior and modeling: drops, streams, shear and mixing layers, jets and sprays. *Prog. Energ. Combust.* **26** (46), 329 – 366.

Bellan, J. 2006 Theory, modeling and analysis of turbulent supercritical mixing. *Combust. Sci. Technol.* **178** (1-3), 253–281.

Branam, R. & Mayer, W. 2002 Length scales in cryogenic injection at supercritical pressure. *Exp. Fluids* **33** (3), 422–428.

Burke, M. P., Chaos, M., Ju, Y., Dryer, F. L. & Klippenstein, S. J. 2012 Comprehensive H2/O2 kinetic model for high-pressure combustion. *Int. J. Chem. Kinet.* **44** (7), 444–474.

Candel, S., Herding, G., Synder, R., Scouflaire, P., Rolon, C., Vingert, L., Habiballah, M., Grisch, F. & Pé, M. 1998 Experimental investigation of shear coaxial cryogenic jet flames. *J. Prop. Power* **14** (5), 826–834.

Chehroudi, B. 2012 Recent experimental efforts on high-pressure supercritical injection for liquid rockets and their implications. *Int. J. Aero. Eng.* **121802**, 31.

Chehroudi, B., Talley, D. & Coy, E. 2002 Visual characteristics and initial growth rates of round cryogenic jets at subcritical and supercritical pressures. *Phys. Fluids* **14**, 850.

Chung, T. H., Ajlan, M., Lee, L. L. & Starling, K. E. 1988 Generalized multiparameter correlation for nonpolar and polar fluid transport properties. *Ind. Eng. Chem. Res.* **27** (4), 671–679.

Chung, T. H., Lee, L. L. & Starling, K. E. 1984 Applications of kinetic gas theories and multiparameter correlation for prediction of dilute gas viscosity and thermal conductivity. *Ind. Eng. Chem. Res.* **23** (1), 8–13.

Cutrone, I., Ihme, M. & Hermann, M. 2006 Modeling of high-pressure mixing and combustion in liquid rocket injectors. *Tech. Rep.*. Proceedings of the Summer Program, Center for Turbulence Research.

Cutrone, L., Palma, P. D., Pascazio, G. & Napolitano, M. 2010 A RANS flamelet/progress-variable method for computing reacting flows of real-gas mixtures. *Comput. Fluids* **39** (3), 485 – 498.

Foust, M. J., Deshpande, M., Pal, S., Ni, T., Merkle, C. & Santoro, R. 1996 Experimental and analytical characterization of a shear coaxial combusting GO2/GH2 flowfield. *AIAA Aerospace Sciences Meeting and Exhibit* (AIAA 96-0646).

Habiballah, M., Orain, M., Grisch, F., Vingert, L. & Gicquel, P. 2006 Experimental studies of high-pressure cryogenic flames on the mascotte facility. *Combust. Sci. Technol.* **178**, 101–128.

Harstad, K. G., Miller, R. S. & Bellan, J. 1997 Efficient high-pressure state equations. *AIChE J.* **43 (6)**, 1605–1610.

Hickey, J.-P., Ma, P. M., Ihme, M. & Thakur, S. 2013 Large eddy simulation of shear coaxial rocket injector: Real fluid effects‘. In *AIAA Joint Propulsion Conference (AIAA 2013-4071)*.

Ihme, M., Cha, C. & Pitsch, H. 2005 Prediction of local extinction and re-ignition effects in non-premixed turbulent combustion using a flamelet/progress variable approach. *P. Comb. Inst.* **30**, 793–800.

Khalighi, Y., Nichols, J. W., Ham, F., Lele, S. & Moin, P. 2010 Unstructured large eddy simulation for prediction of noise issued from turbulent jets in various configurations. In *AIAA Aeroacoustics Conference*.

Lacaze, G. & Oefelein, J. C. 2012 A non-premixed combustion model based on flame structure analysis at supercritical pressures. *Combust. Flame* **158**, 2087–2103.

Lelle, S., Okongo, N. A., Bellan, J. & Harstad, K. G. 2007 Modelling of subgrid-scale phenomena in supercritical transitional mixing layers: an a priori study. *J. Fluid Mech.* **593**, 5791.

Lux, J. & Haidn, O. 2009 Effect of recess in high-pressure liquid oxygen/methane coaxial injection and combustion. *J. Prop. Power* **25** (1), 24–32.

Ma, P. C., Hickey, J.-P. & Ihme, M. 2013 Large-eddy simulations of real-fluid effects in rocket engine combustors. In *Bulletin of the American Physical Society, 66th Annual Meeting of the APS Division of Fluid Dynamics Volume 58, Number 18*.

Masi, E., Bellan, J., Harstad, K. G. & Okongo, N. A. 2013 Multi-species turbulent mixing under supercritical-pressure conditions: modelling, direct numerical simulation and analysis revealing species spinodal decomposition. *J. Fluid Mech.* **721**, 578–626.

Mayer, M. & Tamura, H. 1995 Flow visualization of supercritical propellant injection in a firing LOX/GH2 rocket engine. In *31st AIAA Joint Propulsion Conference and Exhibit (AIAA 95-2433)*.

Mayer, W. O. H., Schik, A. H. A., Vielle, B., Chauveau, C., Goekalp, I., Talley, D. G. & Woodward, R. D. 1998 Atomization and breakup of cryogenic propellants under high-pressure subcritical and supercritical conditions. *J. Prop. Power* **14(5)**, 835842.

Miller, R., Harstad, K. & Bellan, J. 2001 Direct numerical simulations of supercritical fluid mixing layers applied to heptane-nitrogen. *J. Fluid Mech.* **436** (6), 1–39.

Niedermeier, C. A., Mueller, H., Jarczyk, M.-M., Hickel, S., Adams, N. A. & Pfitzner, M. 2013 Large-eddy simulation of turbulent trans- and supercritical mixing. In *AIAA Computational Fluid Dynamics Conference (AIAA 2013-2950)*.

Oefelein, J. C. & Yang, V. 1998 Modeling high-pressure mixing and combustion processes in liquid rocket engines. *J. Prop. Power* **14 (5)**, 843–857.

Okong'o, N. & Bellan, J. 2002*a* Consistent boundary conditions for multicomponent real gas mixtures based on characteristic waves. *J. Comp. Phys.* **176** (2), 330 – 344.

Okong'o, N. & Bellan, J. 2003 Real-gas effects on mean flow and temporal stability of binary-species mixing layers. *AIAA J.* **41 (12)**, 2429–2443.

Okong'o, N. A. & Bellan, J. 2002*b* Direct numerical simulation of a transitional supercritical binary mixing layer: heptane and nitrogen. *J. Fluid Mech.* **464**, 1–34.

Oschwald, M. & Schik, A. 1999 Supercritical nitrogen free jet investigated by spontaneous Raman scattering. *Exp. Fluids* **27** (6), 497–506.

Peng, D.-Y. & Robinson, D. B. 1976 A new two-constant equation of state. *Ind. Eng. Chem. Fundam.* **15(1)**, 59–64.

Pierce, C. & Moin, P. 2004 Progress-variable approach for large-eddy simulation of non-premixed turbulent combustion. *J. Fluid Mech.* **504**, 7397.

Pitsch, H. 2006 A C++ computer program for 0D combustion and 1D laminar flame calculations. (http://www.stanford.edu/group/pitsch/FlameMaster.htm).

Poling, B. E., Prausnitz, J. M. & O'Connell, J. P. 2001 *The properties of gases and liquids*. McGraw-Hill New York.

Prausnitz, J. M., Lichtenthaler, R. & de Azevedo, E. G. 1999 *Molecular thermodynamic of fluid-phase equilibria (third edition)*. Prentice Hall International Press.

Schmitt, T., Selle, L., Ruiz, A. & Cuenot, B. 2010 Large-eddy simulation of supercritical-pressure round jets. *AIAA J.* **48 (9)**, 2133–2144.

Selle, A., Okong'o, N. A., Bellan, J. & Harstad, K. G. 2007 Modelling of subgrid-scale phenomena in supercritical transitional mixing layers: an a priori study. *J. Fluid Mech.* **593**, 5791.

Selle, L. & Schmitt, T. 2010 Large-eddy simulation of single-species flows under supercritical thermodynamic conditions. *Combust. Sci. Technol.* **182** (4-6), 392–404.

Telaar, J., Schneider, G., Hussong, J. & Mayer, W. 2001 Cryogenic jet injection: Description of test case RCM 1. *Tech. Rep.*.

Terashima, H., Kawai, S. & Yamanishi, N. 2011 High-resolution numerical method for supercritical flows with large density variations. *AIAA J.* **49 (12)**, 2658–2672.

Terashima, H. & Koshi, M. 2012 Approach for simulating gas/liquid-like flows under supercritical pressures using a high-order central differencing scheme. *J. Comp. Phys.* **231** (20), 6907 – 6923.

Terashima, H. & Koshi, M. 2013 Strategy for simulating supercritical cryogenic jets using high-order schemes. *Comput. Fluids* **85**, 39–46.

Terrapon, V. E., Pecnik, R., Ham, F. & Pitsch, H. 2010 Full-system RANS of the HyShot II scramjet part 2: Reactive cases. In *Annual Research Briefs*, pp. 69–80. Center for Turbulence Research.

Touber, E. & Sandham, N. D. 2009 Large-eddy simulation of low-frequency unsteadiness in a turbulent shock-induced separation bubble. *Theor. Comput. Fluid Dyn.* **23** (2), 79–107.

Tucker, P. K., Merkle, S. M. M. L., Oefelein, J. C. & Yang, V. 2008 Validation of high-fidelity CFD simulations for rocket injector design. In *AIAA Joint Propulsion Conference & Exhibit (AIAA 2008-5226)*.

Vreman, A. W. 2004 An eddy-viscosity subgrid-scale model for turbulent shear flow: Algebraic theory and applications. *Phys. Fluids* **16 (10)**, 3670–3681.

Yang, B., Cuoco, F. & Oschwald, M. 2007 Atomization and flames in LOX/H2-and LOX/CH4-spray combustion. *J. Prop. Power* **23** (4), 763–771.